Electronic Supplementary Information

Manganite-based memristive heterojunction with tunable non-linear I-V characteristics

Hong-Sub Lee,[a] Hyung-Ho Park*[a] and M. J. Rozenberg*[b,c]

[a] Department of Materials Science and Engineering, Yonsei University, Seodaemun-Ku, Seoul 120-749, Korea. E-mail: hhpark@yonsei.ac.kr

[b] Laboratoire de Physique des Solides, CNRS-UMR 8502 Université Paris-Sud, Orsay 91405, France. E-mail: rozenberg@lps.u-psud.fr

[c] IFIBA-Conicet and Departamento de Física, FCEN, Universidad de Buenos Aires, Ciudad Universitaria Pabellón I, (1428) Buenos Aires, Argentina

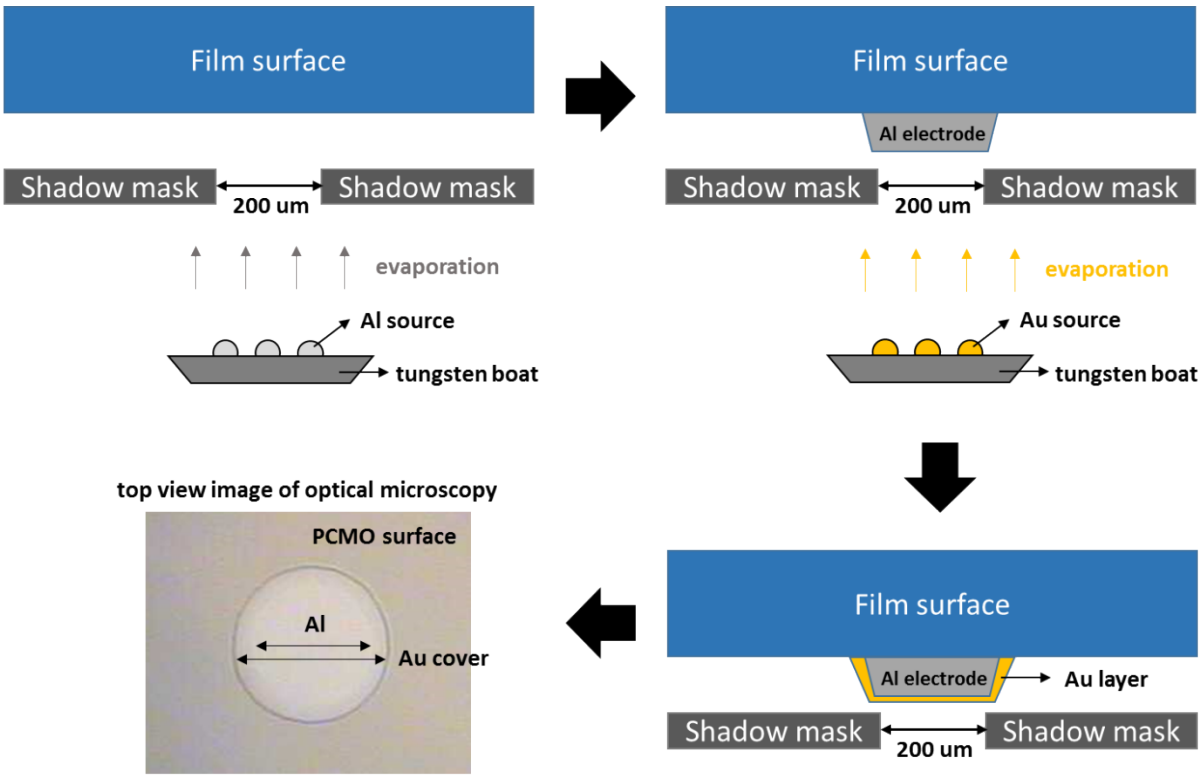

Figure S1. Electrode fabrication method.

Figure S1 shows the electrode (Au (3 nm)/ Al (20 nm)) fabrication method on the PCMO surface. The Al and Au electrodes were deposited in situ and using one mask. We covered the Al electrode with a thin layer of Au (~3 nm) to prevent oxidation from the atmosphere. Due to the ultrathin film, emitted photoelectrons in the underlayer escaped under vacuum.

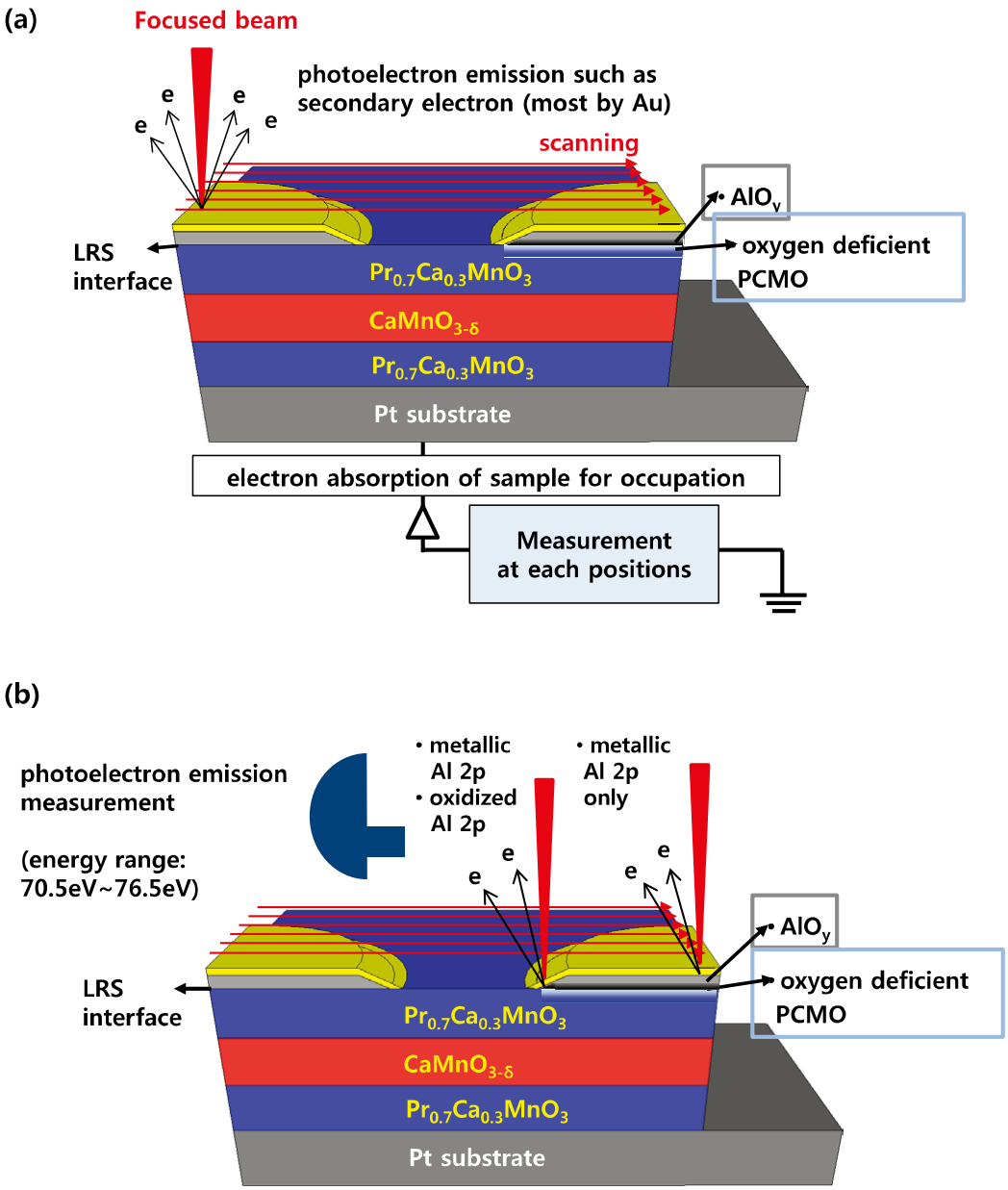

Figure S2. Measurement schemes of (a) sample absorption SPEM and (b) Al 2p photoelectron emission SPEM for Figure 2.

Figure S2(a) shows the measurement method of sample absorption spectromicroscopy (SPEM) for Figures 2(a) and (b). As shown in Figure S2(a), the sample absorbs electrons to occupy the states emptied by photoelectron emission. This study measured the absorption intensity at each position of the sample surface using a focused beam (diameter: 500 nm). Figure S2(b) shows the measurement method of the Al

2p photoelectron SPEM for Figures 2(e) and (f). The photoelectron intensity of the Al 2p energy region was measured at each position of the sample surface using a focused beam. As shown in Figures 2(e) and (f), this study measured the photoelectron signal in six energy sections.

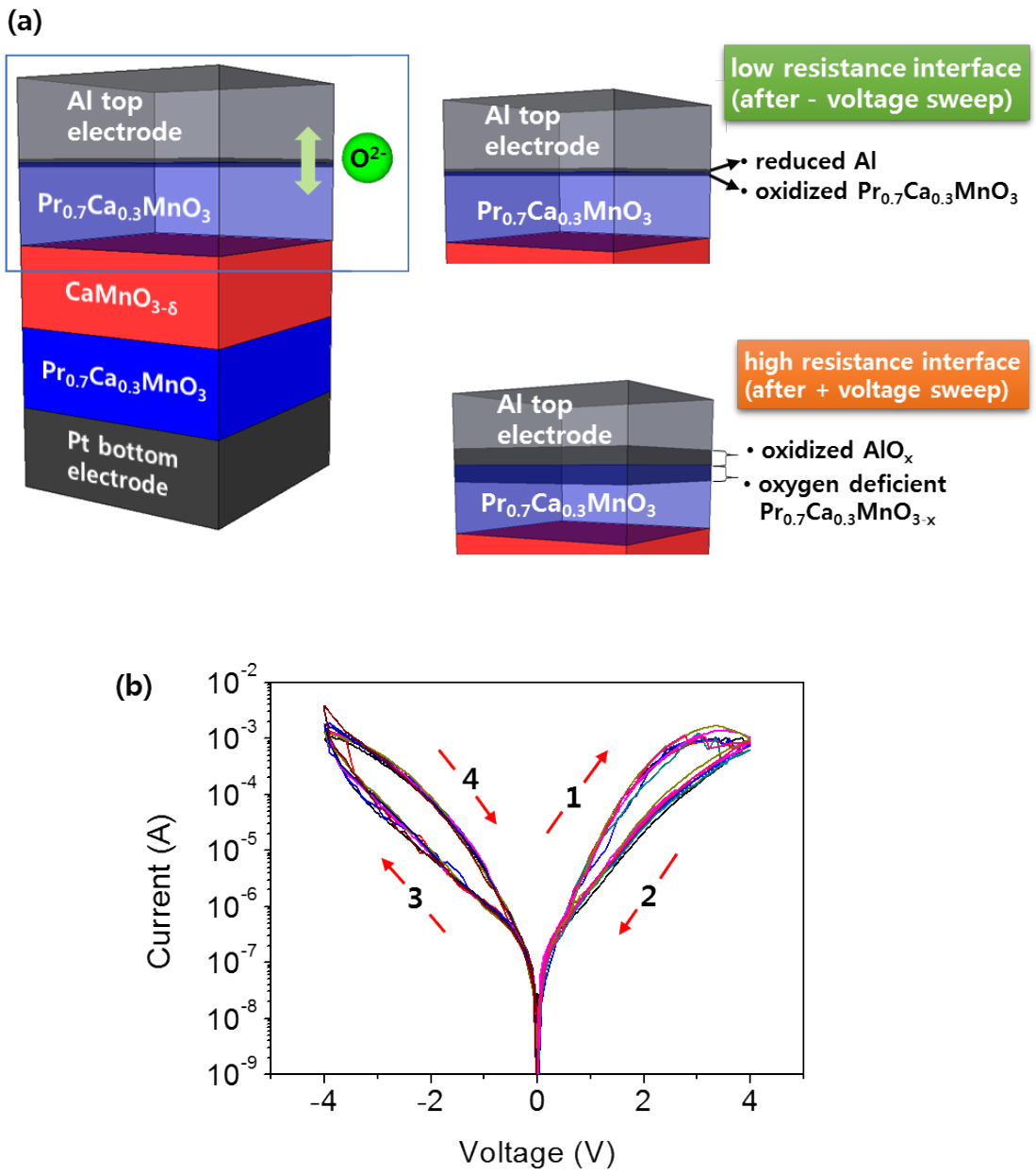

Figure S3. Scheme of (a) a resistive switching mechanism, and (b) resistive switching I-V curves of the interface type operation in the Al/p-type $Pr_{0.7}Ca_{0.3}MnO_3$/n-type $CaMnO_{3-\delta}$/p-type $Pr_{0.7}Ca_{0.3}MnO_3$/Pt structure.

Figure S3(a) is a scheme of the interface type of resistive switching mechanism. Under a positive voltage, oxygen ions move from the PCMO to the reactive top Al electrode, and the oxidized electrode with the reduced PCMO forms HRS. Under a negative voltage, the reverse reaction is induced as LRS switching. Figure S3(b) shows good reproducibility during several RS sweeps.[1,2]

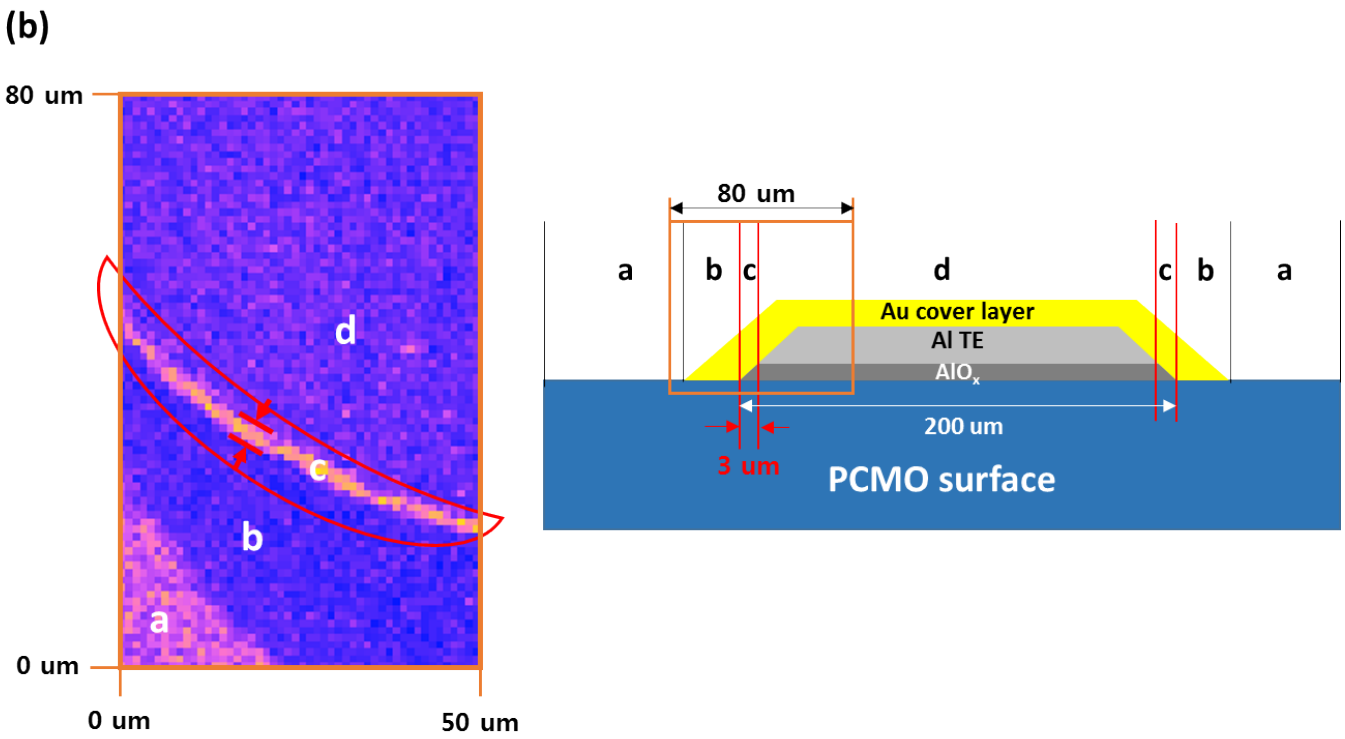

Figure S4. (a) The image of panel 5 in Figure 2f (left), and a scheme of the cross-section of an electrode (right).

Figure S4a shows an analysis of panel 5 (HRS) of Figure 2f from the main text. It shows the signal of the photoelectrons emitted from oxidized Al 2p. Notice the strong intensity of the 'c' region, which should pass through the Au cover layer. As shown in the scheme of the device geometry, oxidation of the Al TE was achieved.

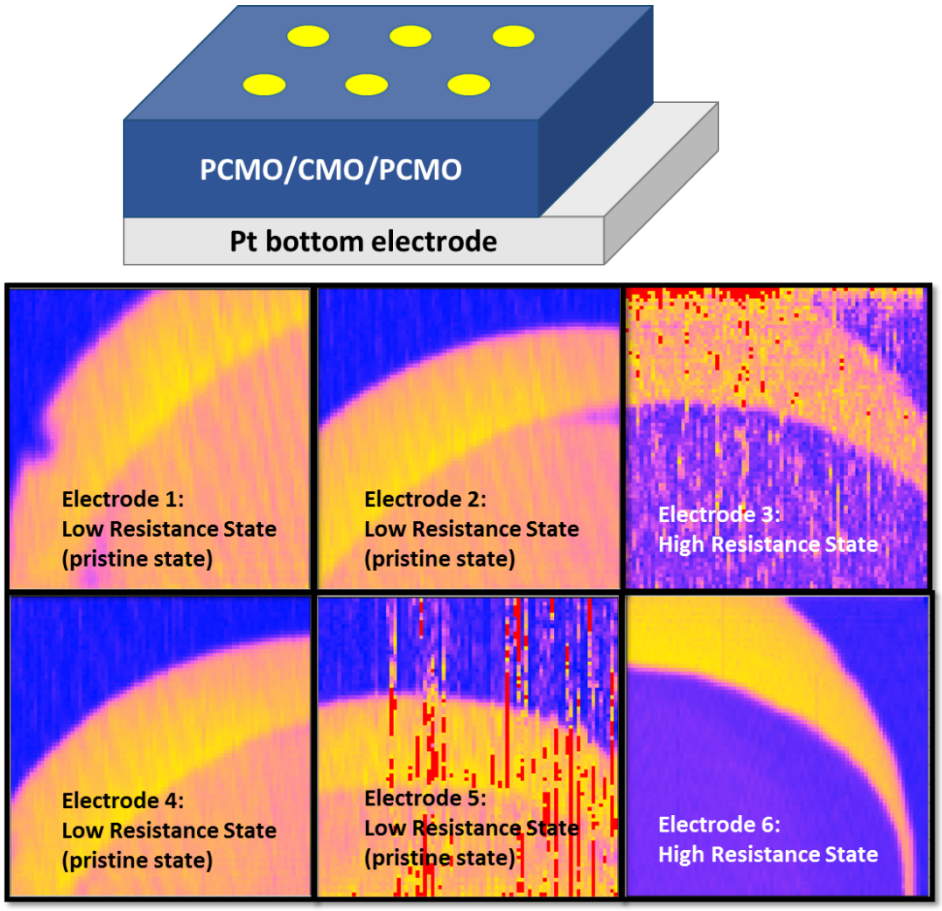

Figure S5. Sample current data of SPEM of six electrodes using the NEXAFS measurement system.

This study determined the uniformity of six electrodes including LRS and HRS electrodes as shown in Figure S5. (The SPEM images of electrodes 3 and 5 included noise from external vibration.) The electrodes 4 and 6 of Figure S5 were used for Figure 2a and b.

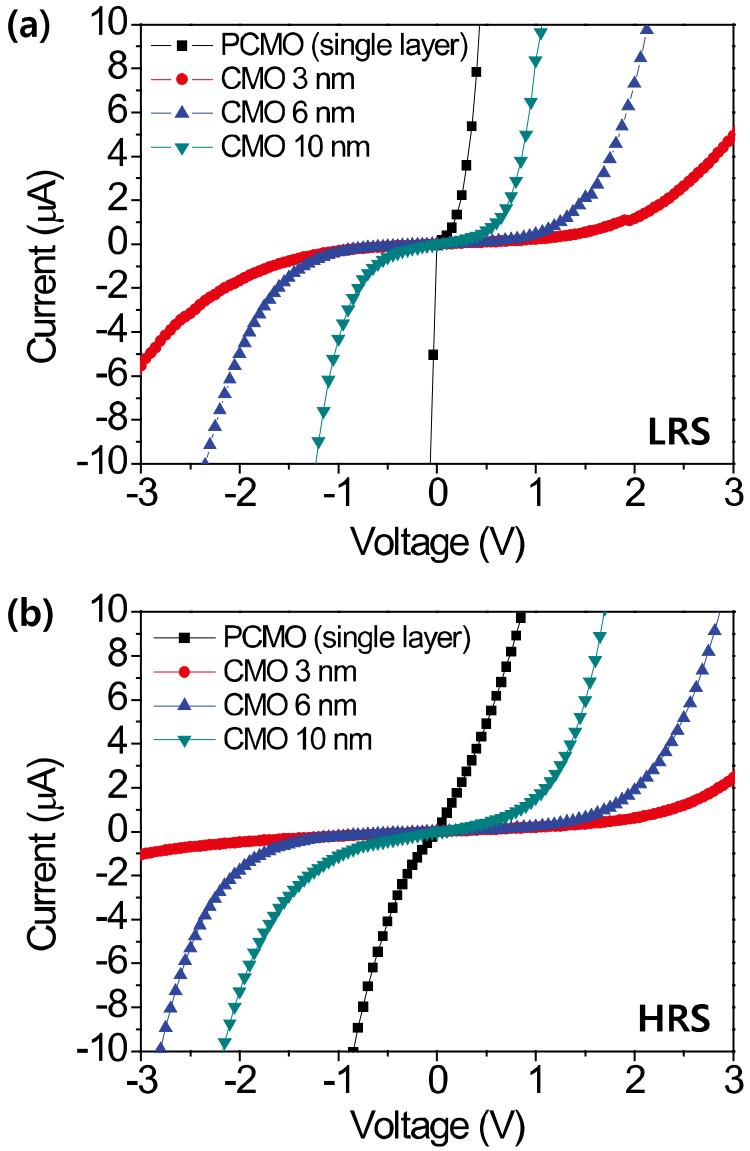

Figure S6. I-V characteristics of (a) LRS and (b) HRS of single-layer PCMO and PCMO/CMO (3 nm, 6 nm, 10 nm)/PCMO structures on a linear scale.

Figure S6 corresponds to the linear scale current-voltage characteristics of a PCMO (30 nm) single-layer film and three kinds of triple-layer films, PCMO/CMO (3 nm)/PCMO, PCMO/CMO (6 nm)/PCMO, and PCMO/CMO (10 nm)/PCMO: (a) and (b) represent LRS and HRS, respectively.

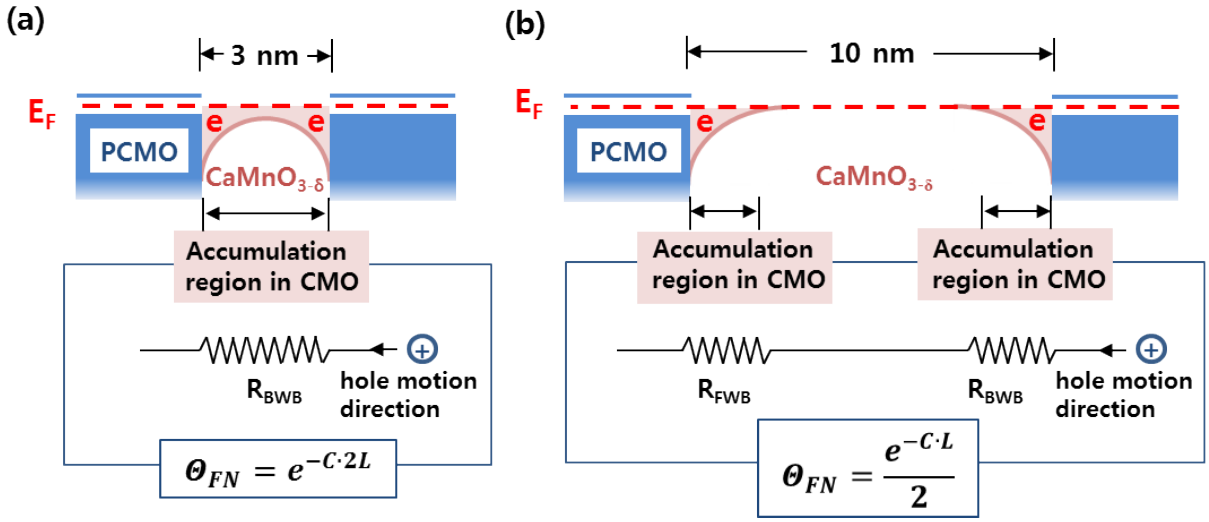

Figure S7. Schematic band diagram and the simplified F-N tunneling probability of the (a) PCMO/CMO(3 nm)/PCMO and (b) PCMO/CMO(10 nm)/PCMO devices.

Upon external voltage application, one barrier in the hole motion is backward (BWB), and the other is forward (FWB). They are connected in series, as shown in Figure S7. Therefore, in the CMO 10 nm sample, the total barrier resistance is the sum of R_{BWB}+R_{FWB}. The resistance values are proportional to the F-N tunneling probability Θ_{FN}, which can be estimated as for a triangle barrier.[3]

$$\Theta_{FN} = exp\left(-\frac{4\sqrt{2qm^*}}{3\hbar}\phi_B^{1/2}L\right) \quad (2)$$

where L is the length of the depletion layer, ϕ_B is the barrier height, q is the carrier charge, and m* is the effective mass. Gathering the parameters that remain constant in all three systems, $\Theta_{FN} = \exp(-C{\cdot}L)$ can be expressed with a constant C. Thus, in the case of the 10 nm CMO layer, $R_{10} \propto 2/\Theta_{FN} = 2/\exp(-C{\cdot}L)$ can be estimated since the two barriers can be considered in series (this should provide an upper limit, since it is likely that R_{BWB} dominates the resistance). On the other hand, in the case of the 3 nm CMO layer, the result is calculated as $R_3 \propto 1/\Theta'_{FN} = 1/\exp(-C{\cdot}2L)$, where Θ'_{FN} is the tunneling probability through an

effectively thicker barrier with a width of approximately *2L*. This is due to the merging of the two depletion regions within the very thin CMO layer. Hence, with respect to the previous case, we can rationalize the apparently paradoxical exponential suppression of the current of the thinner CMO layer hetero-structure. The exponential term largely suppressed the tunneling current. Moreover, when we consider that R_{BWB} is much larger than R_{FWB}, the thicker BWB of the CMO 3 nm film can effectively reduce the F-N tunneling current.

References

1 H. S. Lee, S. G. Choi, H.-H. Park and M. J. Rozenberg, *Sci. Rep.* 2013, **3**, 1704.

2 A. Herpers, C. Lenser, C. Park, F. Offi, F. Borgatti, G. Panaccione, S. Menzel, R. Waser and R. Dittmann, *Adv. Mater.* 2014, **26**, 2730.

3. R. H. Fowler and L. W. Nordheim, *Proc. R. Soc.*

London Ser. A 1928, **119**, 173.